Broadly neutralizing SARS-CoV-2 antibodies through epitope-based selection from convalescent patients

Romain Rouet[1,2*†], Jake Y. Henry[1,2†], Matt D. Johansen[3†], Meghna Sobti[2,4†], Harikrishnan Balachandran[5,6], David B. Langley[1,2], Gregory Walker[567], Helen Lenthall[1,2], Jennifer Jackson[1,2], Stephanie Ubiparipovic[1,2], Ohan Mazigi[1,2], Peter Schofield[1,2], Deborah L. Burnett[1,2], Simon H. J. Brown[8], Marianne Martinello[5,6], Bernard Hudson[9], Nicole Gilroy[10], Jeffrey J. Post[7], Anthony Kelleher[5,6], Hans-Martin Jäck[11], Christopher C. Goodnow[1,2], Stuart G. Turville[5,6], William D. Rawlinson[5,7], Rowena A. Bull[5,6‡], Alastair G. Stewart[2,4‡], Philip M. Hansbro[7‡] and Daniel Christ[1,2*‡]

[1]Garvan Institute of Medical Research, Sydney NSW, Australia

[2]UNSW Sydney, St Vincent's Clinical School, Faculty of Medicine, Sydney NSW, Australia

[3]Center for Inflammation, Centenary Institute and University of Technology Sydney, Sydney NSW, Australia

[4]Victor Chang Cardiac Research Institute, Sydney NSW, Australia

[5]UNSW Sydney, School of Medical Sciences, Faculty of Medicine, Sydney NSW, Australia

[6]Kirby Institute, UNSW Sydney, Sydney NSW, Australia

[7]Prince of Wales Hospital, Sydney NSW, Australia

[8]Molecular Horizons, University of Wollongong, Wollongong, NSW, Australia

[9]Royal North Shore Hospital, Sydney, NSW, Australia

[10]Westmead Hospital, Sydney, NSW, Australia

[11]Division of Molecular Immunology, Friedrich-Alexander University Erlangen-Nürnberg and University Hospital Erlangen, Erlangen-Nürnberg, Germany

* correspondence to Romain Rouet (r.rouet@garvan.org.au) and Daniel Christ (d.christ@garvan.org.au)

† equal contribution; ‡ senior authors

SUMMARY

Emerging variants of concern (VOCs) are threatening to limit the effectiveness of SARS-CoV-2 monoclonal antibodies and vaccines currently used in clinical practice; broadly neutralizing antibodies and strategies for their identification are therefore urgently required. Here we demonstrate that broadly neutralizing antibodies can be isolated from peripheral blood mononuclear cells (PBMCs) of convalescent patients using SARS-CoV-2 receptor binding domains (RBDs) carrying epitope-specific mutations. This is exemplified by two human antibodies, GAR05, binding to epitope class 1, and GAR12, binding to a new epitope class 6 (located between class 3 and class 5). Both antibodies broadly neutralize VOCs, exceeding the potency of the clinical monoclonal sotrovimab (mAb S309) by orders of magnitude. They also provide potent prophylactic and therapeutic *in vivo* protection of hACE2 mice against viral challenge. Our results indicate that exposure to Wuhan SARS-CoV-2 induces antibodies that maintain potent and broad neutralization against emerging VOCs using two unique strategies: either by targeting the divergent class 1 epitope in a manner resistant to VOCs (ACE2 mimicry, as illustrated by GAR05 and mAbs P2C-1F11/S2K14); or alternatively, by targeting rare and highly conserved epitopes, such as the new class 6 epitope identified here (as illustrated by GAR12). Our results provide guidance for next generation monoclonal antibody development and vaccine design.

52 **INTRODUCTION**

53 The coronavirus SARS-CoV-2, the causative agent of the global COVID-19 pandemic,
54 has resulted in the death of over 6 million people worldwide [1]. Upon SARS-CoV-2
55 infection, the human adaptive immune response generates antibodies against the viral
56 spike surface glycoprotein[2]. Most of the neutralizing antibodies bind the spike receptor
57 binding domain (RBD), and in particular class 1 and 2 epitopes within the receptor
58 binding motif (RBM), directly blocking interaction with the human angiotensin
59 converting enzyme receptor 2 (ACE2) [3-6]. Such RBD- and RBM-targeted antibodies
60 are also generated upon vaccination [7], but often lack neutralization potential against
61 emerging variants of concern (VOCs) [8-10]. More recently, broadly neutralizing
62 antibodies have been identified that bind outside the RBM region [11-15]. Such antibodies
63 generally bind to regions conserved among sarbecoviruses (class 3, 4 and 5 epitopes)
64 and are expected to be more resilient to VOCs. However, it is also evident that such
65 antibodies are rare in most vaccinated individuals and convalescent patients [5,14].

66

67 In addition to vaccination, the use of recombinant antibodies has proven successful for
68 therapy and prevention of COVID-19 and several monoclonal antibodies have obtained
69 regulatory approval, and have shown particular promise in immunocompromised
70 individuals and the elderly [16-18]. However, increased resistance to antibody
71 neutralization is being observed for SARS-CoV-2 VOCs, especially for variants
72 carrying mutations within the RBM region (including Beta and Omicron variants) [8-10].
73 To overcome such resistance, research has focused on the development of broadly
74 neutralizing antibodies, such as sotrovimab (S309), which targets the class 3 epitope,
75 which is conserved in sarbecoviruses [19]. In addition, antibody cocktails, targeting

multiple non-overlapping epitopes on the surface of the RBD have been developed to overcome resistance [20,21].

Here we outline a strategy based on the sorting of convalescent patient B cells in an epitope-specific manner, in combination with structural characterization by X-ray crystallography, cryo-electron microscopy (cryo-EM), live virus neutralization and animal models. Using recombinant RBD proteins carrying epitope-specific mutations, we identified neutralizing antibodies binding to diverse epitope classes. Our approach identified a panel of three non-overlapping antibodies (GAR05, GAR12, and GAR20) binding to epitopes classes 1, 6 and 4) that potently neutralize live virus *in vitro* and protect K18-hACE2 mice from intranasal challenge. Although these monoclonals had been isolated from convalescent patients infected early in the pandemic (Wuhan strain), all three potently neutralized the immune evasive Delta VOC, with two of the three (GAR05, GAR12) also potently neutralizing all analyzed Omicron subvariants, highlighting the robustness of the approach. In addition to the previously described class 1-5 epitopes of RBD, our work identified a new epitope class conserved in sarbecoviruses, that we define as class 6, located between class 3 (exemplified by the antibody S309 [19]) and class 5 (exemplified by the antibody S2H97[12]) epitopes. Taken together, our approach identified new broadly neutralizing antibodies from convalescent patients and outlined a new RBD epitope class (class 6), highlighting the potential of the strategy for our understanding of the SARS-CoV-2 antibody response and for future vaccine and therapeutic applications.

101 **RESULTS**

102 **Epitope-based selection of human memory B cells using mutant SARS-CoV-2**
103 **RBDs**

104 We utilized peripheral blood mononuclear cells (PBMCs) from convalescent patients
105 from the COSIN study (New South Wales COVID-19 patient cohort; patients
106 diagnosed by RT-PCR in March 2020 and follow-up samples collected between May
107 and November 2020) [22], at 1- and 4-months post SARS-CoV-2 infection. In order to
108 rapidly identify antibodies binding to different epitopes, we sorted memory B cells
109 based on their capacity to bind to RBD variants carrying epitope class-specific
110 mutations. We initially investigated whether to utilize full spike glycoprotein (trimeric;
111 Wuhan strain [23]; randomly biotinylated) or recombinant RBD (single biotin-tag) to
112 select human memory B cells. Using fluorescently-labeled tetramerized spike and
113 tetramerized RBD, we observed a population of $CD3^{-}CD19^{+}CD20^{+}CD10^{-}IgD^{-}IgG^{+}$ B
114 cells with a high mean of fluorescence intensity (MFI) for both the RBD and spike
115 (albeit lower MFI for spike, Fig. 1A and Supplementary Fig. 1 - Sort 1). Subsequent
116 sorting (Sort 2 and Sort 3; Fig 1A, Supplementary Fig. 1) focused on the use of
117 tetramerized RBD and a series of SARS-CoV-2 RBD mutants to target different epitope
118 classes. We specifically designed RBD mutants to differentiate antibodies blocking the
119 ACE2 interactions and antibodies binding outside the ACE2 binding site. For this
120 purpose, we utilized the following mutant SARS-CoV-2 RBDs: Mut1
121 (T500A/N501A/Y505A), perturbing the ACE2 binding site (targeting class 1 and 2
122 antibody binders); Mut2 (L455A/F456A), blocking a different surface of the ACE2
123 binding site (further targeting further class 1 and 2 binders); and Mut3 (K378S),
124 blocking the CR3022 antibody epitope (targeting class 4 binders) (Fig. 1B) [24]. In
125 addition to mutant RBDs, we also utilized SARS-CoV-1 RBD in order to identify

126 broadly neutralizing antibodies (all RBDs were tetramerized with four distinct
127 fluorescent dyes (Supplementary Fig. 1B). Having observed RBD/spike cross-
128 specificity (Sort 1), the next strategy (Sort 2) employed SARS-CoV-1, SARS-CoV-2
129 and Mut1 and Mut3 RBDs, classifying cells as falling into class 1/2, 4 or unknown
130 epitope classes (Fig. 1 and Supplementary Fig. 1). We consolidated these findings using
131 a third sorting strategy (Sort 3) employing WT SARS-CoV-2, Mut1, Mut2 and Mut3
132 (Fig. 1A and Supplementary Fig. 1 – Sort 3), strengthening delineation of binders that
133 compete with the ACE2 interface.
134
135 **Epitope binning and characterization of human monoclonal antibodies**
136 Following the indexed sorting strategies, human antibody variable regions were
137 amplified from isolated B lymphocytes, cloned into human IgG1 expression vectors,
138 and the encoded monoclonal antibodies expressed and purified [25,26]. For an initial
139 screen, we assessed antibody binding by ELISA and found that 80% (16/20) of the
140 antibodies selected bound to WT SARS-CoV-2 RBD (Supplementary Fig. 2A). We
141 then measured the antibody binding affinities to SARS-CoV-2 RBD by BioLayer
142 Interferometry (BLI), which ranged from 290 nM to 200 pM (Fig. 1C and
143 Supplementary Fig. 2B).
144
145 To further validate class 1/2 antibodies, we performed BLI competition assays with
146 recombinant human ACE2. Amongst the 16 antibodies screened, we identified seven
147 that competed with ACE2 and thus could be considered as class 1/2 candidates
148 (GAR04, 05, 06, 07, 09, 15 and 20) (Supplementary Fig. 3). All but one of these
149 (GAR04) were capable of binding the E484K RBD mutant, a residue pivotal to the
150 binding mode of many class 2 binders [6], hence we tentatively assigned GAR04 as a

151 class 2 binder, while the other six antibodies were assigned as class 1 binders (Fig 1D).
152 IGHV3-53, IGHV1-2 and IGHV3-30 germlines have been commonly observed among
153 class 1 and class 2 SARS-CoV-2 binders[27] , and we also observed these germlines
154 among several of these selected clones (including GAR01, GAR04, and GAR15).
155
156 To further validate class 4 antibodies, we first investigated cross-reactivity with other
157 sarbecovirus RBDs, which are known to be relatively conserved within this epitope
158 (SARS-CoV-1, pangolin CoV and bat RaTG12-CoV) [12,13]. We performed BLI binding
159 experiments with these three sarbecovirus RBDs and identified seven cross-reactive
160 antibodies (GAR01, 03, 11, 13, 14, 16 and 20) (Supplementary Fig. 4). BLI competition
161 assays performed on these cross-reactive antibodies with the class 4 monoclonal
162 antibody CR3022 [28,29](known to bind both SARS-CoV-1 and SARS-CoV-2),
163 confirmed that all, except GAR01 and GAR03, bind to the class 4 epitope
164 (Supplementary Fig. 3). In addition to competing with CR3022, GAR20 also blocked
165 binding of recombinant ACE2 to SARS-CoV-2 RBD, as observed for antibody 3467
166 [14], however this was not observed for the other class 4 antibodies.
167
168 The finding that GAR01 and GAR03 are broadly cross-specific and bind to epitopes
169 conserved in SARS-CoV-2, SARS-CoV-1, pangolin CoV and bat RaTG12-CoV (but
170 do not compete with ACE2 nor CR3022) indicate that these two antibodies may be rare
171 binders falling into the class 5 epitope bin. To investigate this hypothesis, we performed
172 BLI competition assays with the class 5 antibody S2H97 [12], and confirmed that binding
173 of both antibodies is indeed consistent with the class 5 classification (Supplementary
174 Fig. 3).
175

176 Overall, our epitope-binning strategy assigned most of the antibodies to established
177 class 1-5 epitope bins (Fig. 1C)[30]. In addition, antibodies originally sorted into unknown
178 epitope bins were further identified as falling either into epitope class 1/2 (unaffected
179 by T500A/N501A/Y505A and L455A/F456A RBD mutations) or alternately as falling
180 into a new epitope class (class 6, as below).
181
182 Next, we evaluated the capacity of these antibodies to neutralize live virus. We
183 observed that 12/16 of the monoclonal antibodies neutralized SARS-CoV-2 Wuhan
184 (D614G) strain with IC_{50}s ranging from 20 µg/ml to 12 ng/ml (Fig. 1C, Fig. 1D).
185 Several (6/16) antibodies also neutralized the Delta VOC (GAR05, GAR07, GAR09,
186 GAR12, GAR15 and GAR20) (Fig. 1E). Three of these antibodies, GAR05, GAR12
187 and GAR20, were particularly broad in their specificity and neutralized all analyzed
188 variants of concern, with GAR05 neutralizing with IC_{50}s ranging from 115 to 26 ng/ml,
189 and GAR12 and GAR20 neutralizing with IC_{50}s ranging from 255 to 128 ng/ml and 12
190 to 4 µg/ml respectively (Supplementary Fig. 5).
191
192 **GAR05 is a broadly neutralizing class 1 antibody**
193 Based on its potent and broad neutralization potential, antibody GAR05 was further
194 characterized by cryo-EM and X-ray crystallography. For cryo-EM studies, GAR05
195 Fab was incubated with stabilized D614G Wuhan trimeric spike ("VFLIP") [31] at a 3:1
196 molar ratio. The complex was subsequently flash-frozen and examined using cryo-EM
197 (Supplementary Fig. 6 and Supplementary Table 2). The cryo-EM map of GAR05
198 bound to trimeric spike (Fig. 2A, Supplementary Table 1) shows three antibody Fabs
199 bound to the RBD domains of the trimeric spike, where all three RBDs are in the up
200 conformation, consistent with its classification as a class 1 antibody (similarly to what

201 has been observed for antibody C105 [32]). We also solved the crystal structure of GAR05
202 as a Fab fragment in complex with SARS-CoV-2 RBD to 3.2 Å resolution (Fig. 2B,
203 Supplementary Table 2), essentially confirming the binding mode suggested by the
204 cryo-EM map. GAR05 straddles the middle of the saddle-like RBD surface known to
205 interact with the ACE2 receptor (Fig. 2B). The antibody forms a large RBD-interface
206 (~1275 $Å^2$, green surface in Fig. 2D), 815 $Å^2$ of which is contributed by the heavy
207 chain. Heavy-chain complementarity determining regions (CDRs) form a cleft
208 bordered on one side by two finger-like loops (CDRs H1 and H2), opposite a thumb-
209 like loop (extended CDR H3) between which the saddle of the RBD (residues 470-492,
210 Fig. 2C) is bound. CDRs L1 and L3 of the light chain also contact the RBD, forming
211 an additional cleft accommodating the side chain of residue Y505, which projects from
212 an adjacent surface of the RBD (Fig. 2C). The large surface area buried at the interface
213 is at the upper end of what is commonly observed for antibody/antigen interactions [33,34],
214 and is likely reflected by the high affinity of GAR05 towards the RBD (540 pM).
215 However, the surface coverage of GAR05 is in close proximity to multiple positions
216 mutated in various Omicron lineages (Fig. 2D). Rationalisation of why tight binding of
217 GAR05 is nevertheless observed can be made by superposition of the GAR05 complex
218 with cryo-EM and crystal structures of an ensemble of Omicron variants (B1.1.529,
219 BA.2, BA.4/5) from a range of biophysical circumstances (RBD down, RBD up, RBD
220 up and complexed by ACE2, see Supplementary Fig. 7). Of the constellation of
221 positions mutated in Omicron VOCs, eight are likely to interface with GAR05. Four of
222 these (S477N, T478K, E484A and F486V) adorn a loop demonstrating considerable
223 flexibility and which forms one end of the saddle bound by ACE2 (Supplementary Fig.
224 7B). Some positions are mutated to smaller side chains and thus are unlikely to present
225 a steric clash (E484A, F486V, K417N and Y505H; Supplementary Fig. 7, panels B-F).

226 Some positions are mutated to larger side chains albeit presenting in a variety of side
227 chain conformations, some of which might accommodate GAR05 binding (Q493R and
228 N501Y; panel F). Ten hydrogen bonds exist between GAR05 and the RBD (panels G-
229 I). Two of these involve the light chain epitope centered on Y505, both of which will
230 likely be lost by Omicron mutants Y505H and N501Y (panel G). The remaining 8 are
231 heavy-chain centric, 7 involved in contacts with conserved RBD targets (both main-
232 chain and side-chain), and only one will be lost by the E484A mutation (panel I).
233 Hence, the ability of GAR05 to maintain tight binding to Omicron VOCs appears due
234 to combinatorial effects of; coverage of a large epitope surface, the redundancy of
235 heavy and light chains effectively targeting different surfaces (heavy chain targeting
236 the RBD saddle feature, and the light chain targeting the adjacent Y505 feature), the
237 apparent flexibility noted in part of the RBD heavy-chain epitope, the lack of any
238 obvious side-chain mutation likely to present as an unavoidable steric block, and the
239 bulk of hydrogen bonds targeting conserved features.
240
241 The binding mode of GAR05 is similar to that of mAb P2C-1F11, which has been
242 described as an ACE2 mimetic due to sharing extensive steric clash volume with ACE2
243 [35]. A primary difference, however, is the higher affinity and extremely long HCDR3
244 loop of GAR05, which wraps further than P2C-1F11around the RBD saddle targeted
245 by ACE2 (Supplementary Fig. 8, top panels). A further class I targeting antibody,
246 S2K146 [36], has also been described as an ACE2 mimetic as it targets multiple
247 evolutionarily conserved residues utilised by ACE2, and displays broad resistance to
248 VOCs. The overall binding mode of S2K146 resembles that of GAR05, with the notable
249 exception that the orientation of the antibody heavy and light chains are reversed
250 (approximately 180-degree rotation; Supplementary Fig. 8, lower panels).

251

252 **Structural identification of a novel class 6 epitope**

253 We next performed structural studies on two broadly cross-reactive antibodies, GAR03
254 and GAR12, binding conserved epitopes in proximity to that of antibody S2H97 [12].
255 Initial cryo-EM studies using a GAR03-spike mix that had been incubated for 30 min
256 were unsuccessful due to significant aggregation and sample degradation. However, a
257 shorter 1 min incubation of GAR03:spike at a 3:1 ratio improved sample integrity and
258 this preparation was utilized to solve the structure of GAR03 bound to spike
259 glycoprotein (Supplementary Fig. 6 and Supplementary Table 1). Examination of the
260 cryo-EM maps revealed that density could not be observed for the N-terminal domain
261 (NTD) and RBD of one of the three protomers (essentially an S1 domain), with the
262 GAR03 Fab instead occupying the space of the NTD while being bound to the RBD of
263 an adjacent protomer (Fig. 3A). Given that the S2 domain of all three protomers are
264 visible, we hypothesize that binding of GAR03 to an RBD causes the NTD and RBD
265 of an adjacent protomer to be displaced and become flexible, with the averaging
266 methods employed in single particle analysis cryo-EM making their location
267 unidentifiable. Subsequently, we crystalized GAR03 Fab in complex with the RBD and
268 solved the structure by X-ray crystallography to 2.75 Å resolution (Fig. 3A, middle and
269 right-hand panels, and Supplementary Table 2), confirming the binding mode
270 suggested by cryoEM, whereby the bulk of the contact interface is mediated by the
271 antibody light chain, and where the binding epitope is well separated from Omicron
272 variant mutation positions (Fig. 3A, positions highlighted in yellow). Competition
273 binding assays suggested that GAR03 binds to an epitope shared with the class 5
274 antibody S2H97 (Supplementary Fig. 3). Surprisingly, however, mapping of the
275 GAR03 structure onto the S2H97-RBD structure (PDB 7m7w) [12] revealed that,

276 although GAR03 and S2H97 block each other from binding to the RBD, the epitope
277 overlap is minimal (Fig. 3C and 3D – overlap colored green). More specifically, the
278 GAR03 epitope occupies RBD surface extending from the class 5 epitope exemplified
279 by S2H97 to the class 3 epitope site, exemplified by the monoclonal antibody
280 Sotrovimab (S309, PDB 7r6x[12], Fig. 3C – S2H97 in yellow, S309 in pink, and GAR03
281 in shades of blue). This epitope is highly conserved among sarbecoviruses, as
282 highlighted by the cross-reactivity of GAR03 with SARS-CoV-2, SARS-CoV-1,
283 Pangolin CoV and Bat RaTG12-CoV RBD. BLI competition experiments revealed that
284 two other potently neutralizing antibodies, GAR12 and GAR17, competed both with
285 GAR03 and S309 (class 3 epitope) (Supplementary Fig. 9). However, the lack of
286 competition with S2H97 suggests that GAR12 and GAR17 presumably target regions
287 more oriented towards the class 3 epitope site (Fig. 1C). To validate this hypothesis, we
288 solved the crystal structure of the GAR12 Fab in complex with RBD to 2.25 Å
289 resolution (Fig. 3B and Supplementary Table 2). Indeed, GAR12 binds to an epitope
290 on the surface of the RBD that overlaps with S309 and abuts the ACE2 contact surface
291 (Fig. 3B-D, orange cartoon and surfaces). The GAR12 epitope broadly avoids residues
292 mutated in VOCs, thus demonstrating the broad and potent neutralization of this
293 antibody (Fig. 3B). We designate this epitope, shared by GAR03 and GAR12 and
294 spanning a triangular surface between class 5, class 3 and class 1, as class 6 (Fig. 3C).
295
296 Superposition of GAR12, GAR03 and GAR05 antibodies onto the trimeric spike
297 protein with the RBDs in the down position indicates that GAR12 is unimpeded and
298 capable of binding to spike in the fully down position (Fig. 3E – orange Fab cartoons).
299 In contrast, neither GAR03 (blue Fab cartoons) nor GAR05 (green Fab cartoons) can
300 access their respective RBD epitopes in the down position due to steric obstruction from

301 either neighboring N-terminal (both) or RBD domains (of adjacent protomers
302 (GAR05)) within the spike trimer (Fig. 3E).
303
304 **Live virus challenge in the K18-hACE2 mouse model**
305 To further validate monoclonal antibodies identified in this study, live virus challenge
306 experiments were carried out using the K18-hACE2 mouse model of SARS-CoV-2
307 infection in prophylaxis and therapeutic treatments [37,38]. For this purpose, we selected
308 three monoclonal antibodies with broad neutralization of variants of concern (Fig. 1C,
309 Fig. 1E, Supplementary Fig. 5) and non-overlapping epitopes (Supplementary Fig. 9),
310 to enable future application as combination therapy. More specifically, we selected
311 GAR05 for class 1, GAR12 for class 6 and GAR20 for class 4.
312
313 We initially evaluated the antibodies in a prophylaxis model using live SARS-CoV-2
314 virus (Wuhan). Mice were injected intraperitoneally with 30 mg/kg of monoclonal
315 antibody three days prior to challenge with 1 x 10^3 PFU live virus. Mice administered
316 with monoclonal antibodies maintained consistent body weight throughout the
317 challenge compared to mice administered with human IgG1 isotype control (Fig. 4A).
318 Moreover, treatment provided considerable protection from clinical symptoms, with
319 only control mice displaying severe scores (Fig. 4B). Viral titers in lung homogenates
320 from mice treated with monoclonal antibodies were significantly reduced compared to
321 isotype control and generally below the detection limit (Fig. 4C). Investigation of the
322 bronchoalveolar lavage fluids (BALF) revealed that all three treatment groups had
323 statistically significant reductions in inflammatory innate immune cells (macrophages
324 and neutrophils), while maintaining undetectable levels of lymphocytes
325 (Supplementary Fig. 10).

326 In a subsequent study, mice were challenged with Wuhan SARS-CoV-2 in a therapeutic
327 setting, with GAR05 administered post-viral challenge at 30 mg/kg. This experiment
328 revealed that, as had been observed in a prophylactic setting, mice treated with GAR05
329 were fully protected from viral challenge with no measurable weight loss (Fig. 4D),
330 reduction in clinical scores (Fig. 4E) or detectable lung viral titers (Fig. 4F). In a third
331 *in vivo* setting, GAR05 was used as a prophylactic modality (as above), and mice
332 challenged with the Delta (B.1.617.2) VOC. As had been observed for the initial live
333 virus challenge (Wuhan), mice treated with GAR05 were protected from the viral
334 challenge with the Delta VOC: indeed, no measurable reduction of either weight (Fig.
335 4G), clinical scores (Fig. 4H) could be observed, with undetectable viral titers in the
336 prophylaxis group (Fig. 4I).
337
338 Taken together, these findings demonstrate that the monoclonal antibodies developed
339 here, targeting non-overlapping epitopes, broadly and potently protect human ACE2
340 mice from SARS-CoV-2 live virus challenge, highlighting their potential for
341 therapeutic applications.
342
343 **Broad neutralization of Omicron VOCs**
344 The Omicron VOC and its subvariants have caused worldwide outbreaks, highlighting
345 the importance of broad antibody neutralization and mutational resistance [39,40]. When
346 Omicron BA.1 (B.1.1.529) first emerged in November 2021, we and others had shown
347 that only 1/6 monoclonal antibodies in clinical practice fully maintained activity,
348 namely the broadly neutralizing class 3 monoclonal Sotrovimab (S309) [10,41,42]. To
349 assess the potency of GAR05 and GAR12 against Omicron BA.1 and subvariants, we
350 performed *in vitro* neutralization assay using live virus. We observed that GAR05 and

351 GAR12 maintained their activity against the analyzed Omicron VOCs with IC_{50} values
352 ranging from 16.17 ng/ml to 337.6 ng/ml , with IC_{50}s considerably exceeding those of
353 Sotrovimab (S309)[41], particularly for the BA.2 subvariant which is not neutralized by
354 Sotrovimab (Fig. 5B).
355
356 **DISCUSSION**
357 The emergence of new SARS-CoV-2 VOCs, including Omicron variants, with
358 increased transmission and immune evasion, has triggered waves of infection
359 throughout the world [43]. Although existing vaccines remain protective against emerging
360 variants (albeit with reduced effectiveness) [44], the vast majority of monoclonal
361 antibodies do not maintain activity against Omicron VOCs [10,45]. We show here that a
362 sorting strategy based on convalescent patient PBMCs, and RBDs bearing class-
363 specific mutations, can select for sarbecovirus cross-specific antibodies, including
364 those binding to epitopes outside the ACE2-binding site [14,46,47]. Such epitope-based
365 sorting strategies using mutant RBDs may provide an efficient method to rapidly
366 identify specific antibodies against future VOCs using variant RBDs or, alternately,
367 those of ancestral strains. This is exemplified by the work outlined here, based on
368 convalescent patients infected with the ancestral Wuhan strain, which allowed for the
369 identification of antibodies neutralizing a wide range of VOCs. In addition to broadly
370 neutralizing antibodies within each single epitope bin, our strategy allowed for the
371 identification of antibodies in multiple non-overlapping epitope bins, as highlighted by
372 the identification of three non-competing antibodies (GAR05, GAR12 and GAR20)
373 that protect K18-hACE2 mice from live SARS-CoV-2 challenge. This suggests
374 possible future use for combination therapy to increase effectiveness and prevent
375 mutational escape. Using cryo-EM and crystallography, we define a new and highly

376 conserved class 6 RBD epitope on the surface of SARS-CoV-2 RBD, located between
377 class 3 and class 5 epitopes. While the class VI antibodies identified here do not directly
378 occlude binding to the cellular ACE2 receptor, cryo-EM experiments performed on
379 GAR03 indicated rapid disruption of the spike structure upon incubation with antibody,
380 suggesting trimer dissociation as a dominant mode of action (similar to what has been
381 observed for the non-ACE2-blocking antibodies CR3022 (a class IV binder) S2H97 (a
382 class V binder) and COV2-3434 (targeting the NTD) [12,48-50]. This conclusion is further
383 supported by a recently reported antibody, 35B5 [51], which contacts the class VI epitope
384 through unconventional framework interactions (involving outer edges of HCDR2,
385 HCDR3, and framework regions FRH1 and FRH3 – rather than the canonical CDR-
386 mediated interactions reported here – Supplementary Fig. 11). Intriguingly, despite its
387 dramatically different binding mode, 35B5 has also been shown to rapidly disrupt the
388 spike trimer, most likely due to steric issues involving NTD proximity [51], further
389 supporting the notion that interactions with the class VI epitope result in general spike
390 dissociation, independent of specific interaction details. Our results also suggest that
391 exposure to the original Wuhan SARS-CoV-2 RBD (through infection or
392 immunization) induces antibodies in patients that maintain potent and broad
393 neutralization potential against emerging VOCs. This is achieved by either targeting
394 the class 1/2 epitope in a manner resistant to VOCs (as illustrated by GAR05) or
395 alternatively by targeting rare and highly conserved epitopes, such as the novel class 6
396 epitope described here (as illustrated by GAR12), providing important guidance for
397 vaccine design. We conclude that epitope-based selection of SARS-CoV-2 neutralizing
398 antibodies from convalescent patients enables the identification of promising new
399 antibodies and epitopes against emerging variants of concern.

400 **ACKNOWLEDGEMENTS**

401 R.R. acknowledges funding from the Australian Research Council (ACR
402 DE190100985) and from the Garvan Institute of Medical Research (catalytic COVID
403 grant). D.C. acknowledges funding from the Medical Research Future Fund (MRFF
404 MRF2001739) and from the National Health and Medical Research Council (NHMRC
405 APP1157744 and APP1113904). A.G.S. acknowledges funding from the NHMRC
406 (APP1159347). R.A.B. acknowledges funding from the Snow Foundation. P.M.H.
407 acknowledges funding from the NHMRC (APP1175134), MRFF (MRF2007221),
408 NSW RNA Production Network, the Rainbow Foundation and UT. H.M.J.
409 acknowledges grants TRR130 from Deutsche Forschungsgemeinschaft (DFG), grants
410 01KI2043 and COVIM (NaFoUniMedCovid19; FKZ: 01KX2021) from the
411 Bundesministerium für Bildung und Forschung (BMBF), from the Kastner Foundation
412 and grants from the Bayerische Forschungsstiftung and the Bavarian Ministry of Art
413 and Science. Part of this work was performed on the MX2 beamline at the Australian
414 Synchrotron, part of ANSTO. The authors would like to thank the study participants
415 for their contribution to the research. They would like to acknowledge members of the
416 study group: Protocol Steering Committee – Andrew Lloyd (UNSW), John Kaldor
417 (UNSW), Greg Dore (UNSW), Tania Sorrell (Marie Bashir Institute), William
418 Rawlinson (NSWHP), Jeffrey Post (POWH), Bernard Hudson (RNSH), Dominic
419 Dwyer (NSWHP), Adam Bartlett (SCH), Sarah Sasson (UNSW) Nick Di Girolamo
420 (UNSW) and Daniel Lemberg (SCHN). Coordinating Centre - Marianne Byrne
421 (Clinical Trials Manager), Mohammed Hammoud (Post-Doctoral Fellow and Data
422 Manager), Andrew Lloyd (Investigator) and Roshana Sultan (Study co-ordinator). Site
423 Principal Investigators – Jeffrey Post (POWH), Michael Mina (Northern Beaches
424 Hospital), Bernard Hudson (RNSH), Nicky Gilroy (Westmead Hospital), Pam Konecny
425 (St George Hospital), Golo Ahlenstiel (Blacktown Mt Druitt Hospital), Adam Bartlett

(SCHN) and Gail Matthews (St Vincent's Hospital). Site co-ordinators – Dmitrii Shek (Blacktown Mt Druitt Hospital); Katerina Mitsakos (RNSH); Renier Lagunday (POWH); Sharon Robinson (St George Hospital); Lenae Terrill (Northern Beaches Hospital); Neela Joshi, Ying Li and Satinder Gill (Westmead Hospital); Rebecca Hickey and Alison Sevehon (St Vincent's Hospital). We also wish to thank and acknowledge the use of the University of Wollongong Cryogenic Electron Microscopy Facility at Molecular Horizons, the use of the Victor Chang Cardiac Research Institute Innovation Centre, funded by the NSW Government, and the Electron Microscope Unit at UNSW Sydney, funded in part by the NSW Government.

AUTHOR CONTRIBUTIONS

R.R., J.Y.H., R.A.B., D.C. and designed the project; J.Y.H. and H.B. performed human B-cell sorting; R.R. generated SARS-CoV-2 proteins and amplified VH and VL from single B-cells; M.S., S.H.J.B. and A.G.S. performed cryo-EM; D.B.L. performed X-ray crystallography; M.D.J and P.M.H. performed animal experiments; G.W., S.G.T. and W.D.R. performed neutralization experiments; R.R., J.Y.H., H. L., J.J., S.U., O.M. and P.S. performed antibody production and BLI experiments; R.R., J.Y.H., D.B.L. and D.C. wrote the manuscript with input from all other authors.

DECLARATION OF INTERESTS

The authors declare no competing financial interest.

448 **FIGURE LEGENDS**

449

450 **Fig. 1: PBMC single cell sorting strategy and antibody characterization.** A:
451 Memory B cells were selected from convalescent patient PBMCs by gating on $CD3^-$
452 $CD19^+CD20^+CD10^-IgD^-IgG^+$ cells and single cells sorted by binding to fluorescently
453 labeled SARS-CoV-2 RBD or trimeric spike initially (left panel). In addition, using B:
454 mutant RBD protein (mutations colored in orange), single cells were sorted based on
455 FACS epitope bins. Red dots represent the B cells for which monoclonal antibodies
456 were amplified and characterized. C: Monoclonal antibodies analyzed, showing affinity
457 for SARS-CoV-2 RBD (Wuhan strain), neutralization potential and epitope class
458 (initial FACS epitope bin and validation). nn = non neutralizing. C: *In vitro*
459 neutralization of live SARS-CoV-2 virus (n=4).

460

461 **Fig. 2: Structural characterization of the broadly neutralizing class 1 antibody**
462 **GAR05.** A: Cryo-EM structure of GAR05 Fab bound to trimeric spike (3.27 Å
463 resolution) showing full antibody Fab occupancy of all the RBDs in the "up"
464 conformation. B: Structure of GAR05 bound to SARS-CoV-2 RBD based on the X-ray
465 crystal structure, outlining the antibody bound to the ACE2 "saddle" of the RBD. C:
466 Interaction of the CDR regions of the VH and VL domains with the RBD saddle and
467 the Y505 side chain of the RBD. D: Comparison of the ACE2 interface on the surface
468 of RBD and the GAR05 epitope, showing high overlap within the ACE2 saddle region.
469 The large, buried surface area of GAR05 (1275 $Å^2$) indeed blankets many key residues
470 identified in VOCs, colored in yellow, yet remarkably still binds all VOCs with
471 potency.

472

473 **Fig. 3: Structural identification of a novel class 6 epitope.** A: Cryo-EM structure of
474 spike trimer (three shades of grey surface) complexed with GAR03 (blue cartoon and
475 transparent surface) revealing a single GAR03 antibody Fab bound to trimeric spike
476 (resolution 3.39 Å). Binding displaces the S1 domain (N-terminal domain and RBD) of
477 one of the protomers (disordered and not visible in the cryo-EM map), with the GAR03
478 Fab binding to the RBD of the adjacent protomer. Middle and right panels show two
479 perspectives of the RBD-GAR03 crystal structure. The binding interface is dominated
480 by the GAR03 light chain (light blue cartoon; CDRs L1, L2 and L3) with more minor
481 contribution from the heavy chain (dark blue; CDR H3). The ACE2 interface of the
482 RBD (grey surface and cartoon) is shaded black, whilst Omicron VOC mutation
483 positions are indicated by yellow sticks and surface, and N343 linked carbohydrate is
484 also shown as sticks (CHO) B: Crystal structure of GAR12 (heavy and light chains
485 colored dark and light orange) in complex with RBD (grey cartoon and surface, with
486 ACE2 interface colored black, and Omicron VOCs colored yellow). Two perspectives
487 are shown. C: Global juxtaposition of GAR03 (blue surfaces) and GAR12 (orange
488 surfaces) with class 5 representative S2H97 (yellow) and class 3 representative S309
489 (pink) shown against the RBD surface (grey, and black indicating the RBD-ACE2
490 interface). D: RBD-interface comparisons. Left and middle panels including GAR03
491 (blue) and S2H97 (yellow) and their overlap (green). The right panel additionally
492 includes the GAR12 (orange) and S309 interfaces (pink), and their overlap (red). E.
493 Spike trimer (three shades of grey surface) presented with all three RBDs in the down
494 conformation (PDB entry 6xm5) as viewed down the approximate 3-fold axis (left and
495 middle panels); docked Fabs (middle panel) GAR03 (blue cartoons), GAR05 (green
496 cartoons), GAR12 (orange cartoons), as well as the primary helix from ACE2 (yellow

497 cartoon). Modelling indicates that only GAR12 is capable of binding to spike with RBD
498 in the down conformation (right panel, viewed from the side).
499
500 **Fig. 4: Protection of K18-hACE2 mice from live viral challenge.** Animals were
501 injected interperitoneally with 30 mg/kg of GAR05, GAR12, GAR20 or human IgG1
502 isotype control on -3 dpi prior to viral challenge for prophylactic studies (A-C,G-I) or
503 +1 dpi post challenge for therapeutic studies (D-F). Mice were challenged (d0) with
504 $1x10^3$ PFU of intranasal Wuhan SARS-CoV-2 (A-C n=4, D-F n=6) or Delta VOC
505 (B.1.167.2) (G-I n=6) virus and monitored for 6 days, and euthanized (d6) for tissue
506 collection. Measurements of weight (percentage loss from initial weight, A/D/G),
507 clinical score (weight loss, eye closure, appearance of fur and posture, and respiration,
508 B/E/H), and viral titers (lung homogenates; plaque assay, C/F/I) shown. Error bars
509 represent standard error of the mean (SEM).
510
511 **Fig. 5: Neutralization of the Omicron VOCs.** A: SARS-CoV-2 neutralization (live
512 virus), Wuhan (A.2.2), Omicron VOCs BA1, BA2, BA5 (n=4). B: IC_{50} values (ng/ml)
513 reported for S309, GAR05 and GAR12 on Wuhan and Omicron VOCs. nn = non-
514 neutralizing. Error bars represent standard deviation (SD).
515
516
517 **METHODS**
518 **Antigen production and purification**
519 DNA encoding SARS-Cov-2 RBD (residues 319-541) was gene synthesized
520 (Genscript) and cloned into the pCEP4 mammalian expression vector (Invitrogen)
521 encoding a N-terminal IgG leader sequence and C-terminal Avi- and His-tag. RDB
522 mutants were generated by site-directed mutagenesis and splice-overlapping PCR.

523 Plasmids were transfected into Expi293 cells (Thermo Scientific) according to the
524 manufacturer's protocol and the protein expressed for 7 days at 37°C, 8% CO_2. Cell
525 cultures were clarified by centrifugation, dialyzed with PBS and the protein captured
526 with Talon resin (Thermo Scientific). The RBDs were eluted with 150 mM imidazole
527 in PBS, dialyzed with PBS and the purity assessed by visualization on SDS-PAGE. The
528 protein concentration was determined by measuring the Abs_{280nm}. For biotinylation of
529 the Avi-tag, the proteins were buffer exchanged into 20 mM HEPES pH 7.5 + 50 mM
530 NaCl using Zeba Spin desalting columns (Thermo Scientific). Then 10 mM ATP, 10
531 mM $MgCl_2$, 150 µM D-biotin and 3 µM BirA enzyme (purified in-house) in 50 mM
532 bicine buffer pH 8.3 was added to the protein and incubated for 1 h at 30°C. The
533 biotinylated protein was finally buffer exchanged back into PBS and the concentration
534 determined by measuring the Abs_{280nm}. The plasmid encoding the Wuhan SARS-CoV-
535 2 spike protein with C-terminal trimerization domain and His tag was kindly provided
536 by the Krammer lab (BEI Resources). The plasmid encoding the D614G VFLIP spike
537 protein with a C-terminal trimerization domain and Strept-tag was kindly provided by
538 the Saphire lab (La Jolla Institute of Immunology). The spike plasmids were transfected
539 into ExpiCHO and the protein expressed for 7 days at 32°C, 8% CO_2. After expression,
540 culture media were clarified by centrifugation and dialysed against 50 mM Tris pH 7.5
541 + 150 mM NaCl, and the Wuhan spike protein was purified using Talon Resin (Thermo
542 Scientific) while the D614G VFLIP spike was purified on a StrepTrap XT column (GE
543 Healthcare), according to the manufacturer's protocols. The spike proteins were further
544 purified on a Superose 6 gel filtration column (GE Healthcare) in 25 mM Tris pH 7.5
545 + 150 mM NaCl using an AKTA Pure FPLC instrument (GE Healthcare) to isolate the
546 trimeric protein (and remove S2 pre-fusion protein for the Wuhan spike). Finally, the
547 fractions containing the protein were concentrated using Amicon concentrators

548 (Merck), the protein concentration determined by measuring Abs_{280nm} and purity
549 assessed by visualization on SDS-PAGE gel. The spike protein was biotinylated using
550 EZ-Link NHS-PEG4-Biotin reagent (Thermo Scientific) as follows. Purified spike
551 protein was buffer exchanged into PBS using equilibrated Zeba Spin columns. The
552 protein concentration was determined and the spike biotinylated with EZ-Link NHS-
553 PEG4-Biotin at a 10:1 biotin-to-protein molar ratio for 30 min at room temperature.
554 Free biotin was removed from the spike by repeating the buffer exchange step in a
555 second Zeba Spin column equilibrated with 25 mM Tris pH 7.5 + 150 mM NaCl.
556
557 **Human B-cell sorting**
558 SARS-CoV-2 specific memory B cells were characterized and sorted via flow
559 cytometric tetramer assay essentially as previously described [2]: biotinylated SARS-
560 CoV-2 RBD (including mutant variants), spike and SARS-CoV-1 RBD were incubated
561 with Streptavidin-APC (BD), Streptavidin-PE (BD), Streptavidin-BB515 (BD) or
562 BV650-PE (BD) at a 4:1 molar ratio. Streptavidin conjugated fluorophores were titrated
563 onto biotinylated antigen in $1/10^{th}$ volume increments for 10 min per increment at 4°C.
564 Cryopreserved PBMCs from five convalescent patients were thawed and suspended in
565 pre-warmed RPMI-1640 media containing 10% FBS (sigma), 2 mM L-glutamine, 50
566 IU/ml penicillin and 50 µg/ml streptomycin. A maximum of $1x10^7$ cells were
567 resuspended in Fixable Viability Stain 700 (BD) diluted to 1:1000 in PBS and incubated
568 at 4°C for 20 min. Cells were washed twice with FACS buffer (PBS + 0.1% BSA) and
569 incubated with Human Fc block (5µl per $2x10^6$ cells; BD) at room temperature for 10
570 min. Cells were then washed twice with FACS buffer and resuspended in RBD or spike
571 tetramers at 1µg/ml (per tetramer) and incubated at 4°C for 30 min and washed twice
572 more with FACS buffer. Cells were finally suspended in a cell surface staining mix

573 containing (per test): 50 µl brilliant staining buffer (BD), 5 µl anti-human CD21
574 BV421, 5 µl anti-human IgD BV510, 5 µl anti-human CD19 BV711, 5 µl anti-human
575 CD20 APC-H7, 8 µl anti-human IgG BV786, 2 µl anti-human CD27 PE-CF594, 2 µl
576 anti-human CD38 PE-Cy7 and 0.5µl anti-human CD3 BB700 (all antibodies sourced
577 from BD). Surface staining incubation was performed at 4°C for 30 min, washed twice
578 and resuspended in FACS buffer for sorting. Immunophenotyping and index sorting
579 was performed on a BD FACSAria III where a minimum of 300,000 events were
580 acquired for each sample. Data analysis was performed using FlowJo version 10.7.1
581 (FlowJo LLC).
582
583 **Monoclonal antibody production and purification**
584 Sorted single B cells were collected into 96-well PCR plates containing 2 µL of Triton
585 X-100 (0.1%), dNTPs (5 nmol), oligo-dT primer (2.5 pmol) and RNAse inhibitor (1U
586 – Clontech). cDNA generation and amplification was performed following the
587 SmartSeq2 approach [26]. DNA encoding the antibody variable domains was amplified
588 by nested-PCR following the Tiller protocol [25]. DNA encoding VH and VL domains
589 were cloned into pCEP4 vectors encoding human IgG1 and light chains. After
590 validation by Sanger sequencing, plasmids were transfected into ExpiCHO (Thermo
591 Scientific) according to the manufacturer's protocol (1 µg DNA/ml of cells; 2:1 ratio
592 of heavy chain to light chain; following the maximum titer protocol). After 14 days,
593 cell culture media was clarified by centrifugation and the IgG captured using Protein G
594 resin (Genscript). The IgG were eluted from the Protein G resin using 100 mM glycine
595 pH 3.0, dialyzed with PBS and the purity assessed by visualization on SDS-PAGE. For
596 Fab production, the DNA encoding the VH domain was cloned into an in-house human
597 CH1 pCEP4 vectors with a C-terminus His tag. The production was performed in

598 ExpiCHO as for IgG. After 14 days, the cell culture media was clarified by
599 centrifugation, dialyzed against PBS and the Fab captured using Talon resin. The Fab
600 was eluted with 150 mM imidazole in PBS, dialyzed with PBS and the purity assessed
601 by visualization on SDS-PAGE. ACE2 fused to human IgG1 Fc domain was gene
602 synthesized (Genscript) and cloned into pCEP4. Expression was carried out in Expi293
603 cells for 7 days at 37°C, 8% CO_2. After expression, the ACE2 Fc fusion protein was
604 purified by Protein G resin as for human monoclonal antibody.
605
606 **Monoclonal antibody ELISA**
607 Maxisorp plates were coated with SARS-CoV-2 RBD at 2 µg/ml in carbonate coating
608 buffer overnight at 4ºC. The following day, plates were washed twice with PBS and
609 blocked in 4% milk in PBS-T (0.1% Tween 20) for 2 h. Plates were washed 3x with
610 PBS-T and incubated with the monoclonal antibodies diluted to 100 µg/ml in PBS for
611 1 h. Plates were then washed 3x with PBS-T and incubated with HRP-conjugated goat
612 Anti-human IgG/M antibody (Abcam) for 1h. Plates were finally washed 2x with PBS-
613 T and 1x with PBS and incubated with TMB substrate (Perkin Elmer) until the reaction
614 was quenched HCl. Plates were read at Abs 450nm (ClarioStar – BMG Labtech).
615
616 **Monoclonal antibody affinity measurements and competition assays by biolayer**
617 **interferometry (BLI)**
618 Purified monoclonal antibodies were buffer exchanged into PBS using equilibrated
619 Zeba Spin columns. The protein concentration was determined and the antibodies
620 biotinylated by incubating for 30 min at room temperature with EZ-Link NHS-PEG4-
621 Biotinylation reagent (Thermo Scientific) at a 10:1 biotin-to-protein ratio. Free biotin
622 was removed by repeating the buffer exchange step in a second Zeba Spin column

623 equilibrated with PBS. Affinity of interactions between biotinylated antibodies and
624 purified soluble RBD proteins were measured by Biolayer Interferometry (BLItz,
625 ForteBio). Streptavidin biosensors were rehydrated in PBS containing 0.1% BSA for 1
626 h at room temperature. Biotinylated antibody was loaded onto the sensors "on-line"
627 using an advanced kinetics protocol, and global fits were obtained for the binding
628 kinetics by running associations and dissociations of RBD proteins at a suitable range
629 of molar concentrations (2-fold serial dilution ranging from 800 nM to 50 nM). The
630 global dissociation constant (K_D) for each 1:1 binding interaction was determined using
631 the BlitzPro 1.2.1.3 software. For competition assays, RBD at 400 nM was pre-
632 incubated with competitor (ACE2 Fc or unconjugated antibody) at 1 μM for 10 min at
633 room temperature.
634
635 **SARS-CoV2 neutralization assay**
636 Serial 2-fold dilutions of test monoclonal antibody were prepared, and neutralization
637 assay was performed in Vero E6 cells (HEK293T cells over-expressing the human
638 ACE2 receptor for the Delta VOC), as previously described [52].
639
640 **X-ray crystallography**
641 Antibody Fab fragments were purified further via size-exclusion chromatography using
642 an S200 increase 10/30 column (GE Healthcare) equilibrated with 25 mM Tris (pH
643 8.0), 200 mM NaCl. C-terminally His-tagged SARS-CoV-2 RBD (residues 333-528)
644 was expressed and purified as for the other RBDs. Fab and RBD were
645 stoichiometrically combined and concentrated to approximately 5 mg/ml. Solutions
646 were combined with an equal volume (2 μL) of well solution in a vapor diffusion
647 hanging drop crystallization format. For the RBD-GAR05 complex, the well solution

648 comprised 100 mM citrate pH 4.25, 500 mM LiCl and 13% (w/v) PEG 6000. For the
649 RBD-GAR12 complex, the well solution comprised 100 mM of the MMT buffer
650 system (pH 6.6) (Molecular Dimensions; comprising malic acid, 2-ethanesulfonic acid
651 and trisaminomethane), and 19% (w/v) PEG6K. To facilitate crystallization this
652 complex also included an additional antibody Fab (10G4) which binds to a different
653 epitope of the RBD (to be described elsewhere; Mazigi et al). For the RDB-GAR12
654 complex the well solution comprised 100 mM ammonium citrate (pH 5.5), 20% (w/v)
655 PEG3350. Crystals were flash frozen in liquid nitrogen with no cryoprotection regime.
656 Diffraction data were collected at the Australian Synchrotron on beamline MX2 using
657 a Dectris Eiger X16M detector. For all crystals a 360° sweep of data were deconvoluted
658 into 3600 x 0.1° oscillation images which were indexed and integrated by XDS [53].
659 Space groups were determined with Pointless [54] and scaling and merging performed
660 with Aimless [55], both components of CCP4 [56]. Structures were determined by
661 molecular replacement using Phaser [57], using generic human Fab fragments (containing
662 kappa light chain for Fabs GAR05, GAR12 and 10G4, and containing a lambda light
663 chain for GAR03) and SARS-CoV-2 RBD as search models. All structures contained
664 one complex (1:1, or 1:1:1 for GAR03) in the asymmetric unit. Structure refinement
665 was performed using Refmac [58] then phenix.refine [59] between rounds of manual
666 inspection and model adjustment using Coot [60]. The electron density for many parts of
667 the GAR05 model, in particular, was poorly defined, commensurate with the low
668 resolution and very high B-factors, hence refinement employed a combination of
669 reference model and secondary structure restraints, however some of the best density
670 exists at the interface between the antibody and the RBD, providing confidence in the
671 Fab-RBD juxtaposition. Model validation was performed using the Molprobity server

672 [61]. Diffraction data and model refinement statistics are shown in Supplementary Table
673 1.
674
675 **Cryo-electron microscopy**
676 For sample preparation, D614G VFLIP spike trimer and Fab (molar ratio of 1:3) was
677 incubated at room temperature for either 30 min (GAR05 or 1 min (GAR03) before
678 application to holey gold grids and freezing. 3.5 µl of each sample was applied to
679 1.2/1.3 UltrAuFoil grids (Quantifoil) which had been glow-discharged for 1 min at 15
680 mA in an EasiGlow (Pelco). Plunge freezing was performed using a Vitrobot Mark IV
681 (Thermo Scientific) with 0 blot force, 4 s blot time and 100% humidity at 22 °C. Grids
682 were initially screened on a Talos Arctica Electron Microscope (Thermo Scientific) and
683 assessed for particle concentration, integrity, and ice thickness. For final data
684 collection, grids were transferred to a Titan Krios Electron Microscope (Thermo
685 Scientific) operating at 300 kV equipped with a BioQuantum K2 (Gatan) with the slit
686 set to 20 ev. Movies were recorded using EPU with a calibrated pixel size of 1.08 Å, a
687 total dose of 50 electrons spread over 50 frames and a total exposure time of 5 s. All
688 processing was performed in cryoSPARC [62]. Initial particles were picked using the
689 "blob" protocol, and these 2D classified to create templates to pick the datasets.
690 Extracted particles were subjected to multiple rounds of 2D classification, *ab initio*
691 reconstruction and heterogenous refinement to sort the particles into discrete structures
692 (Supp. Fig. 6). In the case of the D614G VFLIP spike trimer bound to GAR03, focussed
693 refinement was utilised on the region corresponding to GAR03:RBD in order to
694 increase the detail in this area (Supp. Fig. 6). An atomic model for GAR03 Fv was
695 generated using ABodyBuilder [63], the constant domains CH1 and lambda CL added
696 using PDB ID 7m3i [64], and fitted into the focussed map. This model was combined with

697 an atomic model for the entire spike complex (PDB ID 6xlu [65]), introducing the D614G
698 VFLIP mutations and removing regions with little to no density. This model was then
699 used to create a combined map (with the focussed and unfocussed maps) in Phenix [66]
700 and the model was fitted/refined using Coot [60], ISOLDE [67] and Phenix. Supp. Fig. 6
701 provides a summary of the data collection and refinement statistics.
702
703 **Animal experiments**
704 All mouse experiments were performed according to ethical guidelines as set out by the
705 Sydney Local Health District (SLHD) Animal Ethics and Welfare Committee, which
706 adhere to the Australian Code for the Care and Use of Animals for Scientific Purposes
707 (2013) as set out by the National Health and Medical Research Council of Australia.
708 SARS-CoV-2 mouse infection experiments were approved by the SLHD Institutional
709 Biosafety Committee. For Wuhan SARS-CoV-2 prophylaxis assays, 4 female
710 hemizygous K18-hACE2 mice (B6.Cg-Tg(K18-hACE2)2Prlmn/J, stock Nb. 034860,
711 Jackson Lab) were injected on day -3 (prior to intranasal viral challenge with 1 x
712 10^3 PFU of Wuhan SARS-CoV-2 (Isolate AUS/VIC01/2020)) intraperitoneally with
713 30mg/kg for each individual antibody (GAR05, GAR12, GAR20 and a human IgG1
714 isotype control (Bio X Cell) at 3mg/ml in PBS) in a 200 µl volume. For Wuhan SARS-
715 CoV-2 therapeutic assays, 6 female hemizygous K18-hACE2 mice (B6.Cg-Tg(K18-
716 hACE2)2Prlmn/J, stock Nb. 034860, Jackson Lab) were injected on day 1 (post
717 intranasal viral challenge with 1 x 10^3 PFU of Wuhan SARS-CoV-2 (Isolate
718 AUS/VIC01/2020)) intraperitoneally with 30mg/kg GAR05 or a human IgG1 isotype
719 control (Bio X Cell) at 3mg/ml in PBS) in a 200 µl volume. For Delta SARS-CoV-2
720 prophylaxis assays, 6 female hemizygous K18-hACE2 mice (B6.Cg-Tg(K18-
721 hACE2)2Prlmn/J, stock Nb. 034860, Jackson Lab) were injected on day -3 (prior to

722 intranasal viral challenge with 1 x 10^3 PFU of Delta SARS-CoV-2 (B1.617.2))
723 intraperitoneally with 30mg/kg GAR05 and a human IgG1 isotype control (Bio X Cell)
724 at 3mg/ml in PBS) in a 200 µl volume. On day 0, treated mice were moved to the
725 PC3/BSL3 lab and intranasally inoculated with 1 x 10^3 PFU of Wuhan SARS-CoV-2
726 (Isolate AUS/VIC01/2020) or Delta SARS-CoV-2 (B1.617.2) in a 30 µl volume as
727 previously described [38]. Mice were weighed, monitored and scored for clinical
728 symptoms (weight loss, eye closure, appearance of fur and posture, and respiration)
729 daily and any mice that reached the ethical endpoints were humanely euthanised. On
730 day 6, all mice were humanely euthanised. Multi-lobe lungs were tied off and BALF
731 was collected from the single lobe via lung lavage with 1 mL HANKS solution using a
732 blunted 19-gauge needle inserted into the trachea. BALF was centrifuged (300 *g*, 4 °C,
733 7 min), and supernatants collected and snap frozen. Cell pellets were treated with
734 200 µL Red Blood Cell Lysis Buffer (Thermo Scientific) for 5 min, followed by
735 addition of 700 µL HANKS solution to inactivate the reaction and then centrifuged
736 again. Cell pellets were resuspended in 160 µL HANKS solution and enumerated using
737 a haemocytometer (Sigma-Aldrich). Differential cell BALF counts were performed by
738 loading 70 µl of the BALF cell pellet into a cytospin funnel and centrifuging (300×*g*,
739 7 min) and were left to airdry overnight. Following drying, slides were stained using
740 the Quick Dip stain kit (POCD Scientific) as per manufacturer's instructions. Multi-
741 lobe lungs were collected and snap frozen on dry ice. Lung homogenates were prepared
742 fresh, with the third multi-lobe lungs placed into a gentleMACS C-tube (Miltenyi
743 Biotec) containing 2 mL HANKS solution. Tissue was homogenised using a
744 gentleMACS tissue homogeniser, after which homogenates were centrifuged (300×*g*,
745 7 min) to pellet cells, followed by collection of supernatants for plaque assays. The
746 significance of differences between experimental groups was evaluated by one-way

747 analysis of variance (ANOVA), with pairwise comparison of multi-grouped data sets
748 achieved using Tukey's or Dunnett's *post-hoc* test. Differences were considered
749 statistically significant when $p \leq 0.05$.
750
751
752
753

754 **REFERENCES**

755 1 World Health Organization Coronavirus (COVID-19) Dashboard.
756 2 Abayasingam, A. *et al.* Long-term persistence of RBD(+) memory B cells
757 encoding neutralizing antibodies in SARS-CoV-2 infection. *Cell Rep Med* **2**, 100228
758 (2021). https://doi.org:10.1016/j.xcrm.2021.100228
759 3 Seow, J. *et al.* Longitudinal observation and decline of neutralizing antibody
760 responses in the three months following SARS-CoV-2 infection in humans. *Nat*
761 *Microbiol* **5**, 1598-1607 (2020). https://doi.org:10.1038/s41564-020-00813-8
762 4 Noy-Porat, T. *et al.* A panel of human neutralizing mAbs targeting SARS-
763 CoV-2 spike at multiple epitopes. *Nat Commun* **11**, 4303 (2020).
764 https://doi.org:10.1038/s41467-020-18159-4
765 5 Piccoli, L. *et al.* Mapping Neutralizing and Immunodominant Sites on the
766 SARS-CoV-2 Spike Receptor-Binding Domain by Structure-Guided High-Resolution
767 Serology. *Cell* **183**, 1024-1042 e1021 (2020).
768 https://doi.org:10.1016/j.cell.2020.09.037
769 6 Barnes, C. O. *et al.* SARS-CoV-2 neutralizing antibody structures inform
770 therapeutic strategies. *Nature* **588**, 682-687 (2020). https://doi.org:10.1038/s41586-
771 020-2852-1
772 7 Greaney, A. J. *et al.* Antibodies elicited by mRNA-1273 vaccination bind
773 more broadly to the receptor binding domain than do those from SARS-CoV-2
774 infection. *Sci Transl Med* **13** (2021). https://doi.org:10.1126/scitranslmed.abi9915
775 8 Wang, P. *et al.* Increased resistance of SARS-CoV-2 variant P.1 to antibody
776 neutralization. *Cell Host Microbe* **29**, 747-751 e744 (2021).
777 https://doi.org:10.1016/j.chom.2021.04.007
778 9 Wang, P. *et al.* Antibody resistance of SARS-CoV-2 variants B.1.351 and
779 B.1.1.7. *Nature* **593**, 130-135 (2021). https://doi.org:10.1038/s41586-021-03398-2
780 10 Aggarwal, A. *et al.* SARS-CoV-2 Omicron: evasion of potent humoral
781 responses and resistance to clinical immunotherapeutics relative to viral variants of
782 concern. *medRxiv*, 2021.2012.2014.21267772 (2021).
783 https://doi.org:10.1101/2021.12.14.21267772
784 11 Robbiani, D. F. *et al.* Convergent antibody responses to SARS-CoV-2 in
785 convalescent individuals. *Nature* **584**, 437-442 (2020).
786 https://doi.org:10.1038/s41586-020-2456-9
787 12 Starr, T. N. *et al.* SARS-CoV-2 RBD antibodies that maximize breadth and
788 resistance to escape. *Nature* **597**, 97-102 (2021). https://doi.org:10.1038/s41586-021-
789 03807-6
790 13 Onodera, T. *et al.* A SARS-CoV-2 Antibody Broadly Neutralizes SARS-
791 related Coronaviruses and Variants by Coordinated Recognition of a Virus
792 Vulnerable Site. *Immunity* (2021). https://doi.org:10.1016/j.immuni.2021.08.025
793 14 Burnett, D. L. *et al.* Immunizations with diverse sarbecovirus receptor-binding
794 domains elicit SARS-CoV-2 neutralizing antibodies against a conserved site of
795 vulnerability. *Immunity* (2021). https://doi.org:10.1016/j.immuni.2021.10.019
796 15 Rappazzo, C. G. *et al.* Broad and potent activity against SARS-like viruses by
797 an engineered human monoclonal antibody. *Science* **371**, 823-829 (2021).
798 https://doi.org:10.1126/science.abf4830
799 16 Cohen, M. S. *et al.* Effect of Bamlanivimab vs Placebo on Incidence of
800 COVID-19 Among Residents and Staff of Skilled Nursing and Assisted Living
801 Facilities: A Randomized Clinical Trial. *JAMA* **326**, 46-55 (2021).
802 https://doi.org:10.1001/jama.2021.8828

803 17 Chen, P. *et al.* SARS-CoV-2 Neutralizing Antibody LY-CoV555 in
804 Outpatients with Covid-19. *N Engl J Med* (2020).
805 https://doi.org:10.1056/NEJMoa2029849
806 18 Group, R. C. *et al.* Casirivimab and imdevimab in patients admitted to hospital
807 with COVID-19 (RECOVERY): a randomised, controlled, open-label, platform trial.
808 *medRxiv*, 2021.2006.2015.21258542 (2021).
809 https://doi.org:10.1101/2021.06.15.21258542
810 19 Pinto, D. *et al.* Cross-neutralization of SARS-CoV-2 by a human monoclonal
811 SARS-CoV antibody. *Nature* **583**, 290-295 (2020). https://doi.org:10.1038/s41586-
812 020-2349-y
813 20 Ku, Z. *et al.* Molecular determinants and mechanism for antibody cocktail
814 preventing SARS-CoV-2 escape. *Nat Commun* **12**, 469 (2021).
815 https://doi.org:10.1038/s41467-020-20789-7
816 21 Sun, Y. *et al.* Structure-based development of three- and four-antibody
817 cocktails against SARS-CoV-2 via multiple mechanisms. *Cell Res* **31**, 597-600
818 (2021). https://doi.org:10.1038/s41422-021-00497-7
819 22 COSIN.study. https://kirby.unsw.edu.au/project/natural-history-cohort-
820 following-sars-cov-2-infection. (2020).
821 23 Amanat, F. *et al.* A serological assay to detect SARS-CoV-2 seroconversion in
822 humans. *Nat Med* **26**, 1033-1036 (2020). https://doi.org:10.1038/s41591-020-0913-5
823 24 Rouet, R. *et al.* Potent SARS-CoV-2 binding and neutralization through
824 maturation of iconic SARS-CoV-1 antibodies. *MAbs* **13**, 1922134 (2021).
825 https://doi.org:10.1080/19420862.2021.1922134
826 25 Tiller, T. *et al.* Efficient generation of monoclonal antibodies from single
827 human B cells by single cell RT-PCR and expression vector cloning. *J Immunol*
828 *Methods* **329**, 112-124 (2008). https://doi.org:10.1016/j.jim.2007.09.017
829 26 Picelli, S. *et al.* Full-length RNA-seq from single cells using Smart-seq2. *Nat*
830 *Protoc* **9**, 171-181 (2014). https://doi.org:10.1038/nprot.2014.006
831 27 Yuan, M. *et al.* Structural basis of a shared antibody response to SARS-CoV-
832 2. *Science* **369**, 1119-1123 (2020). https://doi.org:10.1126/science.abd2321
833 28 Tian, X. *et al.* Potent binding of 2019 novel coronavirus spike protein by a
834 SARS coronavirus-specific human monoclonal antibody. *Emerg Microbes Infect* **9**,
835 382-385 (2020). https://doi.org:10.1080/22221751.2020.1729069
836 29 Yuan, M. *et al.* A highly conserved cryptic epitope in the receptor binding
837 domains of SARS-CoV-2 and SARS-CoV. *Science* **368**, 630-633 (2020).
838 https://doi.org:10.1126/science.abb7269
839 30 Jette, C. A. *et al.* Broad cross-reactivity across sarbecoviruses exhibited by a
840 subset of COVID-19 donor-derived neutralizing antibodies. *Cell Rep* **37**, 110188
841 (2021). https://doi.org:10.1016/j.celrep.2021.110188
842 31 Olmedillas, E. *et al.* Structure-based design of a highly stable, covalently-
843 linked SARS-CoV-2 spike trimer with improved structural properties and
844 immunogenicity. *bioRxiv*, 2021.2005.2006.441046 (2021).
845 https://doi.org:10.1101/2021.05.06.441046
846 32 Barnes, C. O. *et al.* Structures of Human Antibodies Bound to SARS-CoV-2
847 Spike Reveal Common Epitopes and Recurrent Features of Antibodies. *Cell* **182**, 828-
848 842 e816 (2020). https://doi.org:10.1016/j.cell.2020.06.025
849 33 Davies, D. R. & Cohen, G. H. Interactions of protein antigens with antibodies.
850 *Proc Natl Acad Sci U S A* **93**, 7-12 (1996). https://doi.org:10.1073/pnas.93.1.7
851 34 Ramaraj, T., Angel, T., Dratz, E. A., Jesaitis, A. J. & Mumey, B. Antigen-
852 antibody interface properties: composition, residue interactions, and features of 53

853 non-redundant structures. *Biochim Biophys Acta* **1824**, 520-532 (2012).
854 https://doi.org:10.1016/j.bbapap.2011.12.007
855 35 Ge, J. *et al.* Antibody neutralization of SARS-CoV-2 through ACE2 receptor
856 mimicry. *Nat Commun* **12**, 250 (2021). https://doi.org:10.1038/s41467-020-20501-9
857 36 Park, Y. J. *et al.* Antibody-mediated broad sarbecovirus neutralization through
858 ACE2 molecular mimicry. *Science* **375**, 449-454 (2022).
859 https://doi.org:10.1126/science.abm8143
860 37 Johansen, M. D. *et al.* Animal and translational models of SARS-CoV-2
861 infection and COVID-19. *Mucosal Immunol* **13**, 877-891 (2020).
862 https://doi.org:10.1038/s41385-020-00340-z
863 38 Counoupas, C. *et al.* A single dose, BCG-adjuvanted COVID-19 vaccine
864 provides sterilising immunity against SARS-CoV-2 infection. *NPJ Vaccines* **6**, 143
865 (2021). https://doi.org:10.1038/s41541-021-00406-4
866 39 Dyer, O. Covid-19: South Africa's surge in cases deepens alarm over omicron
867 variant. *BMJ* **375**, n3013 (2021). https://doi.org:10.1136/bmj.n3013
868 40 Pulliam, J. R. C. *et al.* Increased risk of SARS-CoV-2 reinfection associated
869 with emergence of the Omicron variant in South Africa. *medRxiv*,
870 2021.2011.2011.21266068 (2021). https://doi.org:10.1101/2021.11.11.21266068
871 41 Touret, F., Baronti, C., Bouzidi, H. S. & de Lamballerie, X. In
872 vitro evaluation of therapeutic antibodies against a SARS-CoV-2 Omicron
873 B.1.1.529 isolate. *bioRxiv*, 2022.2001.2001.474639 (2022).
874 https://doi.org:10.1101/2022.01.01.474639
875 42 Cameroni, E. *et al.* Broadly neutralizing antibodies overcome SARS-CoV-2
876 Omicron antigenic shift. *bioRxiv* (2021). https://doi.org:10.1101/2021.12.12.472269
877 43 Tao, K. *et al.* The biological and clinical significance of emerging SARS-
878 CoV-2 variants. *Nat Rev Genet* (2021). https://doi.org:10.1038/s41576-021-00408-x
879 44 Lopez Bernal, J. *et al.* Effectiveness of Covid-19 Vaccines against the
880 B.1.617.2 (Delta) Variant. *N Engl J Med* **385**, 585-594 (2021).
881 https://doi.org:10.1056/NEJMoa2108891
882 45 Falcone, M. *et al.* Efficacy of Bamlanivimab/Etesevimab and
883 Casirivimab/Imdevimab in Preventing Progression to Severe COVID-19 and Role of
884 Variants of Concern. *Infect Dis Ther* **10**, 2479-2488 (2021).
885 https://doi.org:10.1007/s40121-021-00525-4
886 46 Feldman, J. *et al.* Naive human B cells engage the receptor binding domain of
887 SARS-CoV-2, variants of concern, and related sarbecoviruses. *Sci Immunol* **6**,
888 eabl5842 (2021). https://doi.org:10.1126/sciimmunol.abl5842
889 47 Shinnakasu, R. *et al.* Glycan engineering of the SARS-CoV-2 receptor-
890 binding domain elicits cross-neutralizing antibodies for SARS-related viruses. *J Exp*
891 *Med* **218** (2021). https://doi.org:10.1084/jem.20211003
892 48 Huo, J. *et al.* Neutralization of SARS-CoV-2 by Destruction of the Prefusion
893 Spike. *Cell Host & Microbe* **28**, 445-454.e446 (2020).
894 https://doi.org:https://doi.org/10.1016/j.chom.2020.06.010
895 49 Dejnirattisai, W. *et al.* Omicron-B.1.1.529 leads to widespread escape from
896 neutralizing antibody responses. *bioRxiv*, 2021.2012.2003.471045 (2021).
897 https://doi.org:10.1101/2021.12.03.471045
898 50 Suryadevara, N. *et al.* An antibody targeting the N-terminal domain of SARS-
899 CoV-2 disrupts the spike trimer. *J Clin Invest* **132** (2022).
900 https://doi.org:10.1172/JCI159062
901 51 Wang, X. *et al.* A potent human monoclonal antibody with pan-neutralizing
902 activities directly dislocates S trimer of SARS-CoV-2 through binding both up and

903 down forms of RBD. *Signal Transduction and Targeted Therapy* **7**, 114 (2022).
904 https://doi.org:10.1038/s41392-022-00954-8
905 52 Tea, F. *et al.* SARS-CoV-2 neutralizing antibodies: Longevity, breadth, and
906 evasion by emerging viral variants. *PLoS Med* **18**, e1003656 (2021).
907 https://doi.org:10.1371/journal.pmed.1003656
908 53 Kabsch, W. Xds. *Acta Crystallogr D Biol Crystallogr* **66**, 125-132 (2010).
909 https://doi.org:10.1107/S0907444909047337
910 54 Evans, P. R. An introduction to data reduction: space-group determination,
911 scaling and intensity statistics. *Acta Crystallogr D Biol Crystallogr* **67**, 282-292
912 (2011). https://doi.org:10.1107/S090744491003982X
913 55 Evans, P. R. & Murshudov, G. N. How good are my data and what is the
914 resolution? *Acta Crystallographica Section D* **69**, 1204-1214 (2013).
915 https://doi.org:doi:10.1107/S0907444913000061
916 56 Winn, M. D. *et al.* Overview of the CCP4 suite and current developments.
917 *Acta Crystallogr D Biol Crystallogr* **67**, 235-242 (2011).
918 https://doi.org:10.1107/S0907444910045749
919 57 McCoy, A. J. Solving structures of protein complexes by molecular
920 replacement with Phaser. *Acta Crystallogr D Biol Crystallogr* **63**, 32-41 (2007).
921 https://doi.org:10.1107/S0907444906045975
922 58 Murshudov, G. N. *et al.* REFMAC5 for the refinement of macromolecular
923 crystal structures. *Acta Crystallogr D Biol Crystallogr* **67**, 355-367 (2011).
924 https://doi.org:10.1107/S0907444911001314
925 59 Afonine, P. V. *et al.* Towards automated crystallographic structure refinement
926 with phenix.refine. *Acta Crystallogr D Biol Crystallogr* **68**, 352-367 (2012).
927 https://doi.org:10.1107/S0907444912001308
928 60 Emsley, P., Lohkamp, B., Scott, W. G. & Cowtan, K. Features and
929 development of Coot. *Acta Crystallogr D Biol Crystallogr* **66**, 486-501 (2010).
930 https://doi.org:10.1107/S0907444910007493
931 61 Chen, V. B. *et al.* MolProbity: all-atom structure validation for
932 macromolecular crystallography. *Acta Crystallogr D Biol Crystallogr* **66**, 12-21
933 (2010). https://doi.org:10.1107/S0907444909042073
934 62 Punjani, A., Rubinstein, J. L., Fleet, D. J. & Brubaker, M. A. cryoSPARC:
935 algorithms for rapid unsupervised cryo-EM structure determination. *Nat Methods* **14**,
936 290-296 (2017). https://doi.org:10.1038/nmeth.4169
937 63 Leem, J., Dunbar, J., Georges, G., Shi, J. & Deane, C. M. ABodyBuilder:
938 Automated antibody structure prediction with data-driven accuracy estimation. *MAbs*
939 **8**, 1259-1268 (2016). https://doi.org:10.1080/19420862.2016.1205773
940 64 Jennewein, M. F. *et al.* Isolation and characterization of cross-neutralizing
941 coronavirus antibodies from COVID-19+ subjects. *Cell Rep* **36**, 109353 (2021).
942 https://doi.org:10.1016/j.celrep.2021.109353
943 65 Zhou, T. *et al.* Cryo-EM Structures Delineate a pH-Dependent Switch that
944 Mediates Endosomal Positioning of SARS-CoV-2 Spike Receptor-Binding Domains.
945 *bioRxiv* (2020). https://doi.org:10.1101/2020.07.04.187989
946 66 Liebschner, D. *et al.* Macromolecular structure determination using X-rays,
947 neutrons and electrons: recent developments in Phenix. *Acta Crystallogr D Struct Biol*
948 **75**, 861-877 (2019). https://doi.org:10.1107/S2059798319011471
949 67 Croll, T. I. ISOLDE: a physically realistic environment for model building
950 into low-resolution electron-density maps. *Acta Crystallogr D Struct Biol* **74**, 519-530
951 (2018). https://doi.org:10.1107/S2059798318002425
952

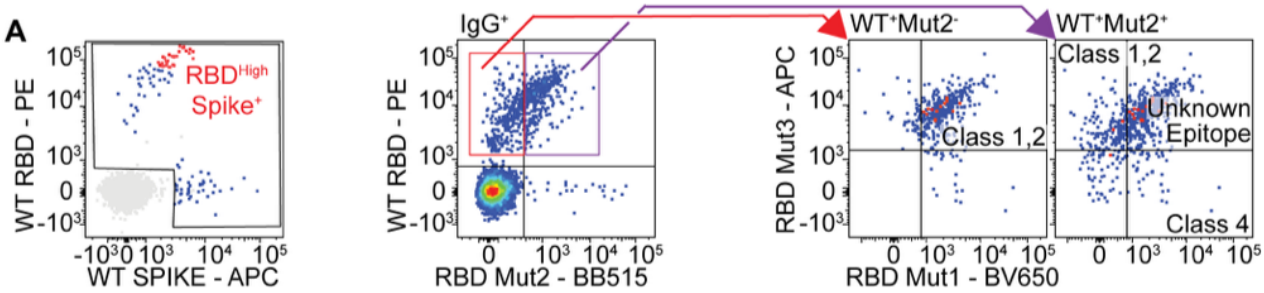

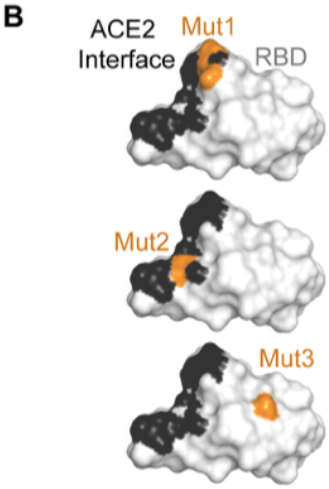

C

Antibody name	Affinity/RBD (nM)	Wuhan IC_{50} (ng/ml)	Delta IC_{50} (ng/ml)	FACS epitope bin	Validated class
GAR01	292	nn	nn	RBD	5,6
GAR03	0.31	>20000	nn	RBD	6
GAR04	23.3	12	nn	RBD	2
GAR05	0.54	28	50	RBD	1
GAR06	37.8	455	8042	RBD	1
GAR07	2.87	287	582	unknown	1
GAR09	1.47	106	113	1,2	1
GAR11	20.6	10000	nn	4	4
GAR12	0.20	182	255	1,2	6
GAR13	0.30	nn	nn	1,2	4
GAR14	2.15	nn	nn	1,2	4
GAR15	1.30	157	74	unknown	1
GAR16	3.28	nn	nn	4,5	4
GAR17	1.95	162	nn	unknown	3,6
GAR18	0.24	14630	nn	unknown	6
GAR20	0.60	5470	3770	4	4

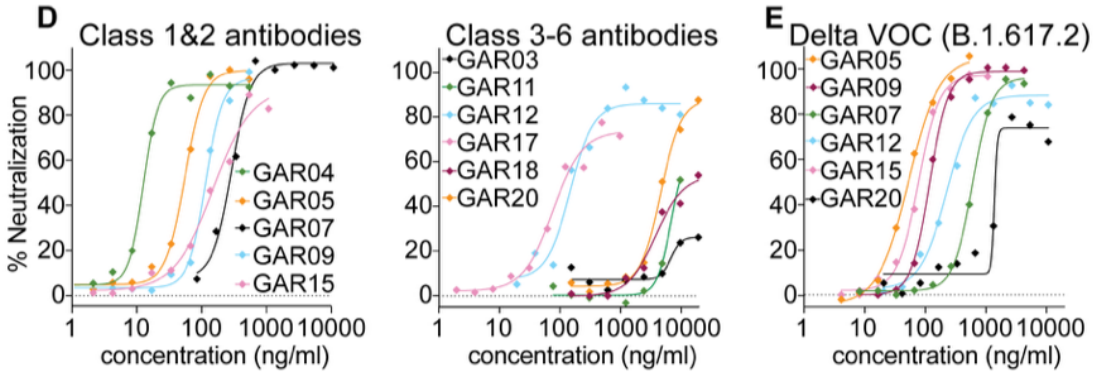

Figure 1

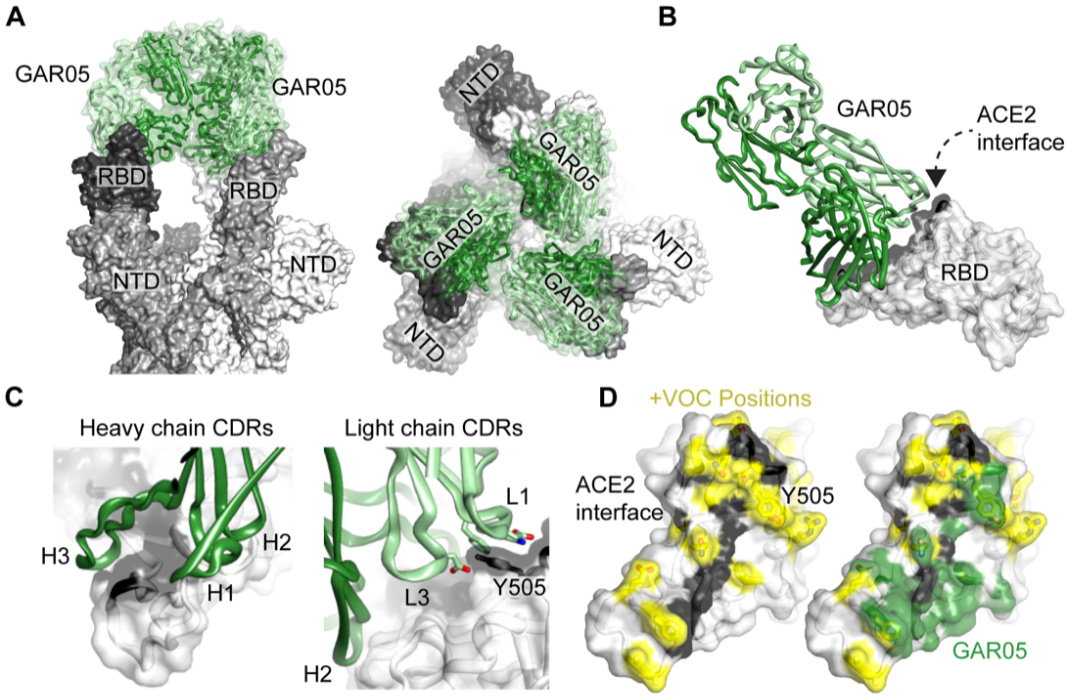
A
GAR05
GAR05
RBD
RBD
NTD
NTD
NTD
GAR05
GAR05
GAR05
NTD
NTD
B
GAR05
ACE2
interface
RBD
C
Heavy chain CDRs
Light chain CDRs
H3
H2
H1
L1
L3
Y505
H2
D
+VOC Positions
ACE2
interface
Y505
GAR05

Figure 2

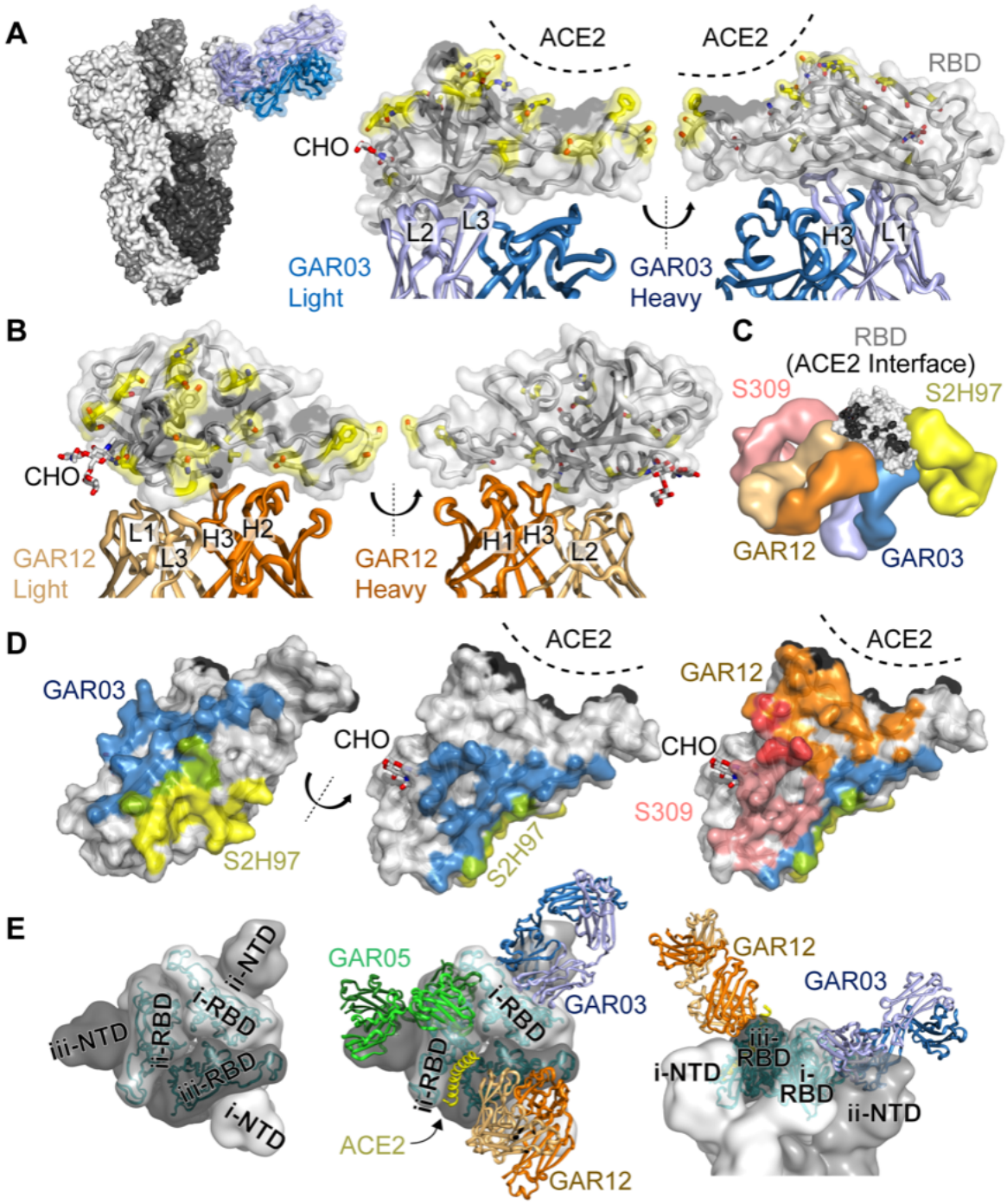
A
ACE2
ACE2
RBD
CHO
L2
L3
GAR03
Light
GAR03
Heavy
H3
L1
B
C
RBD
(ACE2 Interface)
S309
S2H97
CHO
L1
H3
H2
L3
GAR12
Light
GAR12
Heavy
H1
H3
L2
GAR12
GAR03
D
ACE2
ACE2
GAR03
GAR12
CHO
CHO
S309
S2H97
S2H97
E
ii-NTD
i-RBD
ii-RBD
iii-NTD
iii-RBD
i-NTD
GAR05
i-RBD
GAR03
ii-RBD
ACE2
GAR12
GAR12
GAR03
iii-RBD
i-NTD
i-RBD
ii-NTD

Figure 3

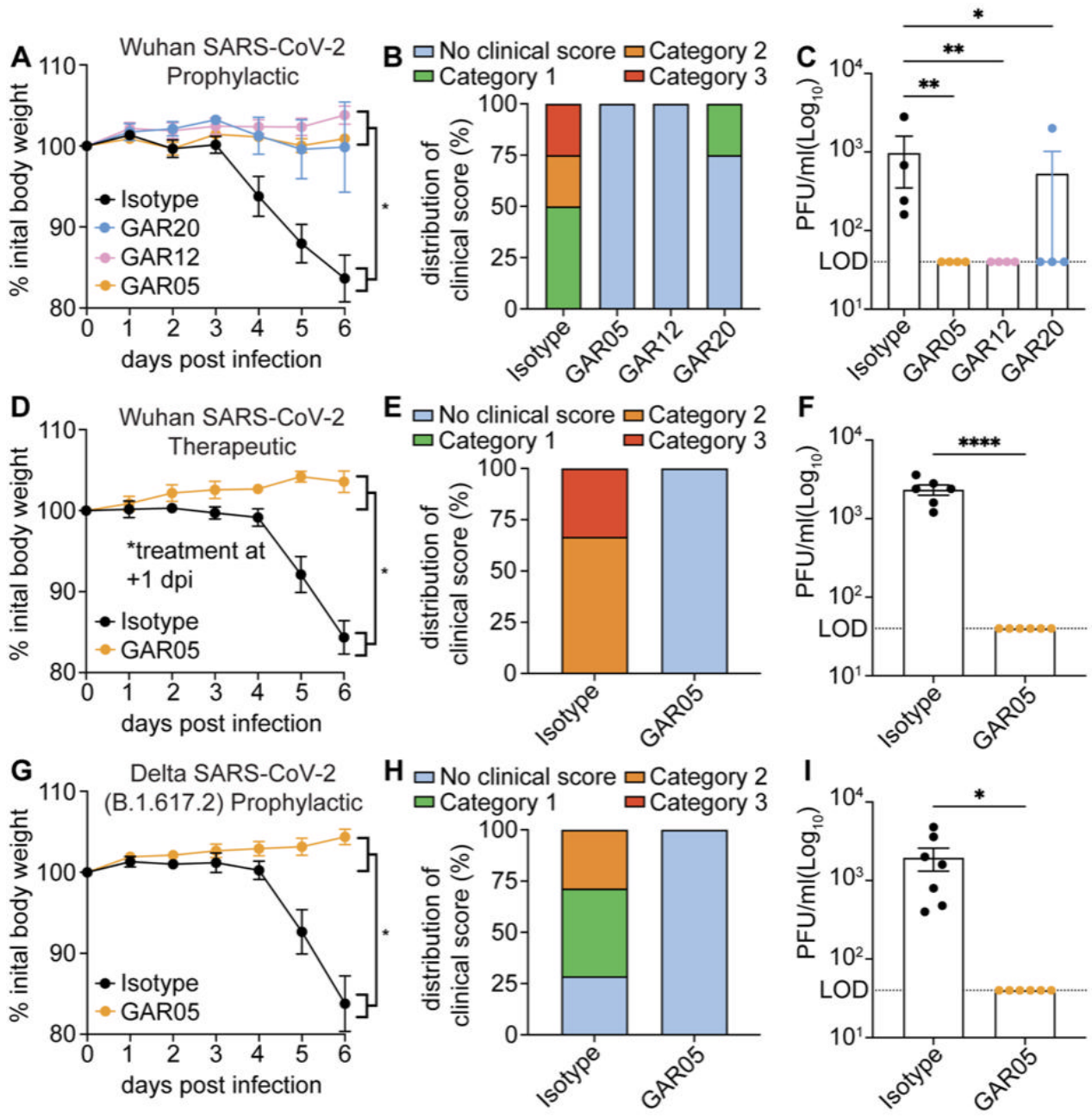
A
Wuhan SARS-CoV-2
Prophylactic
% inital body weight
days post infection
Isotype
GAR20
GAR12
GAR05
B
No clinical score
Category 1
Category 2
Category 3
distribution of clinical score (%)
Isotype
GAR05
GAR12
GAR20
C
PFU/ml(Log10)
LOD
D
Wuhan SARS-CoV-2
Therapeutic
*treatment at +1 dpi
E
F
G
Delta SARS-CoV-2
(B.1.617.2) Prophylactic
H
I

Figure 4

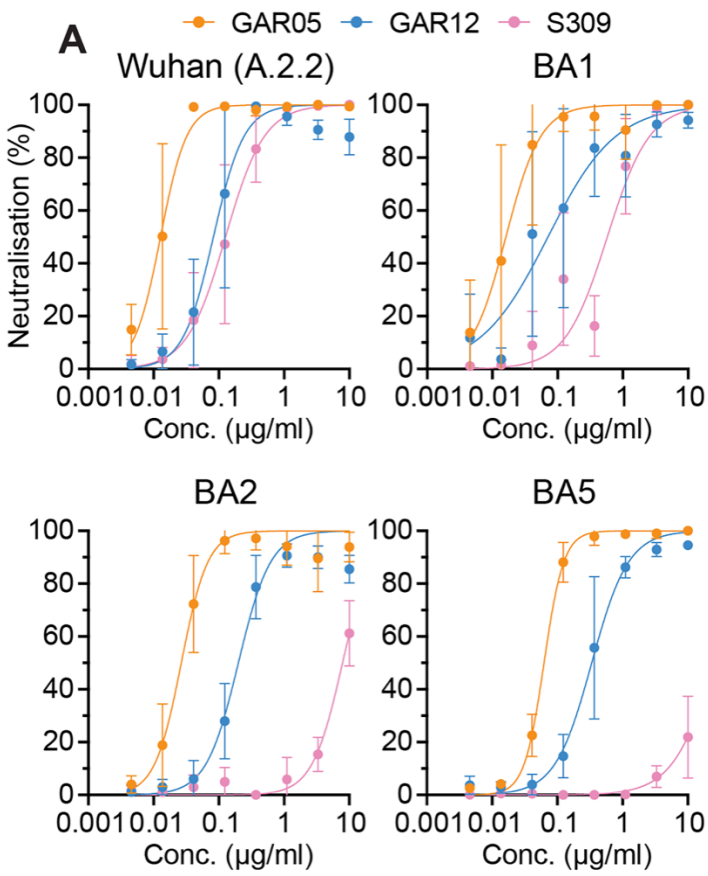

B

IC_{50} (ng/ml)	GAR05	GAR12	S309
Wuhan (A.2.2)	82.45	12.77	132.6
BA1	71.31	16.17	804.6
BA2	198.9	26.58	nn
BA5	337.6	62.59	3826

Figure 5